AGU PUBLICATIONS

Geophysical Research Letters

RESEARCH LETTER
10.1002/2015GL064865

Key Points:
- Vector magnetograms of source ARs of 189 CMEs are analyzed
- The speed of the fastest CMEs produced by ARs increases with twist and magnetic energy parameters
- One of the parameters determines the CME-speed upper limit line better than others

Correspondence to:
S. K. Tiwari,
sanjiv.k.tiwari@nasa.gov

Citation:
Tiwari, S. K., D. A. Falconer, R. L. Moore, P. Venkatakrishnan, A. R. Winebarger, and I. G. Khazanov (2015), Near-Sun speed of CMEs and the magnetic nonpotentiality of their source active regions, *Geophys. Res. Lett.*, *42*, doi:10.1002/2015GL064865.

Received 8 JUN 2015
Accepted 3 JUL 2015
Accepted article online 7 JUL 2015

Near-Sun speed of CMEs and the magnetic nonpotentiality of their source active regions

Sanjiv K. Tiwari[1], David A. Falconer[1,2], Ronald L. Moore[1,2], P. Venkatakrishnan[3], Amy R. Winebarger[1], and Igor G. Khazanov[2]

[1]NASA Marshall Space Flight Center, Huntsville, Alabama, USA, [2]Center for Space Plasma and Aeronomic Research, University of Alabama in Huntsville, Huntsville, Alabama, USA, [3]Udaipur Solar Observatory, Physical Research Laboratory, Udaipur, India

Abstract We show that the speed of the fastest coronal mass ejections (CMEs) that an active region (AR) can produce can be predicted from a vector magnetogram of the AR. This is shown by logarithmic plots of CME speed (from the SOHO Large Angle and Spectrometric Coronagraph CME catalog) versus each of ten AR-integrated magnetic parameters (AR magnetic flux, three different AR magnetic-twist parameters, and six AR free-magnetic-energy proxies) measured from the vertical and horizontal field components of vector magnetograms (from the Solar Dynamics Observatory's Helioseismic and Magnetic Imager) of the source ARs of 189 CMEs. These plots show the following: (1) the speed of the fastest CMEs that an AR can produce increases with each of these whole-AR magnetic parameters and (2) that one of the AR magnetic-twist parameters and the corresponding free-magnetic-energy proxy each determine the CME-speed upper limit line somewhat better than any of the other eight whole-AR magnetic parameters.

1. Introduction

One of the most challenging tasks in the field of modern space research is the prediction of the severity of geomagnetic storms and solar energetic particle storms caused by solar flares and coronal mass ejections (CMEs). Active regions (ARs) on the Sun are the main sources of the biggest flares and most energetic CMEs [*Zirin and Liggett*, 1987; *Subramanian and Dere*, 2001; *Falconer et al.*, 2002; *Venkatakrishnan and Ravindra*, 2003; *Guo et al.*, 2007; *Wang and Zhang*, 2008; *Gopalswamy et al.*, 2010]. The initial speed of CMEs is one of the most important parameters that (among others, e.g., the direction, width and mass of CMEs, orientation, and strength of magnetic field therein) can help forecast the severity of geomagnetic storms and particle storms [see, e.g., *Srivastava and Venkatakrishnan*, 2002; *Gopalswamy et al.*, 2010; *Dumbović et al.*, 2015, and references therein]. The magnetic nonpotentiality of an AR, inferred by, for instance, free magnetic energy proxies and magnetic-twist parameters, is most likely to determine the initial speed of CMEs emanating from the AR. Several other unexplored parameters, e.g., AR lifetime, flux emergence/cancelation [e.g., *Subramanian and Dere*, 2001] might be important as well. Therefore, study of the relationship between properties of the photospheric magnetic field of an AR and the physical properties of the CMEs produced by the AR, e.g., their initial speed, is of great importance for forecasting severe space weather.

Venkatakrishnan and Ravindra [2003] estimated the potential magnetic field energy of 37 ARs from their line-of-sight (LOS) magnetograms and found it to be a reasonable predictor of the speed of CMEs arising from the ARs. The present paper reports a similar but more extensive investigation based on vector magnetograms instead of LOS magnetograms. *Liu* [2007] studied 21 halo CMEs and found a positive correlation of free magnetic energy of ARs with CME speed. CME speed is also found to be correlated with the GOES X-ray magnitude of the coproduced flare [*Ravindra*, 2004; *Burkepile et al.*, 2004; *Vršnak et al.*, 2005; *Gopalswamy et al.*, 2007; *Bein et al.*, 2012]. *Tiwari et al.* [2010] found a good correlation between a twist parameter (spatially averaged signed shear angle: *Tiwari et al.* [2009a] of ARs and the GOES X-ray magnitude of flares produced by the ARs. A comparison of results from *Tiwari et al.* [2010] and *Jing et al.* [2010] suggests that this global twist parameter is strongly correlated with the free magnetic energy of ARs. From the above, one expects twist parameters and free-energy proxies to be determinants of the speed of the CMEs from an AR and therefore determinants of the severity of the resultant geomagnetic storms, based on the results of *Srivastava and Venkatakrishnan* [2002]. In the present analysis, we investigate the relationship between magnetic parameters of ARs (mainly various twist parameters and free-energy proxies) and the initial speed of CMEs arising from the ARs.

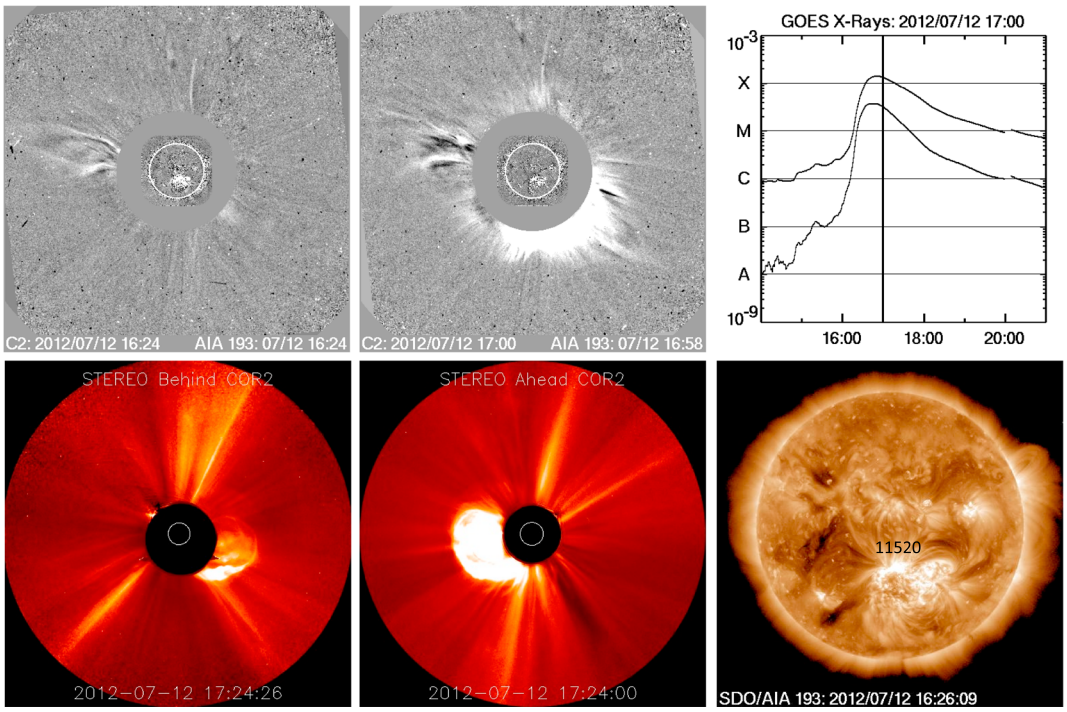

Figure 1. Images illustrating how we verify that a CME comes from an AR or group of ARs. LASCO C2 images, (top left) during the rise of the source AR flare and (top middle) when the CME was clearly visible outside the C2 occulting disk. (top right) A corresponding GOES X-ray plot is shown. (bottom middle) STEREO-A and (bottom left) B images in the bottom row verify that the CME is Earthward directed. (bottom right) An image taken from the AIA 193 Å movie, verifying that the position and NOAA number of the AR responsible for the CME are correct.

Major CMEs emanating from ARs are coproduced with a flare [*Yashiro et al.*, 2008; *Wang and Zhang*, 2008; *Schrijver*, 2009]. Although several investigations have focused on predicting the flares from ARs by measuring various magnetic nonpotentiality parameters [see e.g., *Hagyard et al.*, 1984; *Canfield et al.*, 1999; *Falconer et al.*, 2002; *Georgoulis and Rust*, 2007; *Leka and Barnes*, 2007; *Falconer et al.*, 2009; *Moore et al.*, 2012; *Falconer et al.*, 2014; *Bobra et al.*, 2014, *Bobra and Couvidat*, 2015], a direct link of any of these magnetic parameters to CME parameters has not been established thus far. To establish such a relationship requires (1) a careful manual inspection of which CME comes from which AR and (2) an analysis of vector magnetograms of source ARs within 45 heliocententric degrees of disk center. In the present work, we first generated a list of a large number of CMEs that were observed by the SOHO Large Angle and Spectrometric Coronagraph (LASCO)/C2 coronagraph and were identified with flares in ARs observed by the Solar Dynamics Observatory (SDO). We then manually inspected those CMEs to find the CMEs that came from a clearly identified source AR or sometimes two neighboring ARs. We then calculated different twist parameters and free-energy proxies using vector magnetograms from SDO's Helioseismic and Magnetic Imager (HMI) [*Schou et al.*, 2012; *Hoeksema et al.*, 2014] and studied their relationships to initial CME speeds collected from the LASCO/CME catalog [*Gopalswamy et al.*, 2009].

2. Event Selection and Data Analysis

First, we determined from the online LASCO/CME catalog (http://cdaw.gsfc.nasa.gov/CMElist/) all CMEs that took place between the start of the SDO mission (May 2010) through March 2014 (as far as the LASCO/CME catalog covered at the time of our analysis). We identified all CMEs that had a plane-of-sky width greater than 30° and had a coproduced flare in an AR identified by NOAA. Further, the flaring AR had to be between 45°E to 45°W and the flare occurred (t_{flare}) up to 2 h before the recorded start time till half an hour after the recorded start time of the CME (t_{cme}) in images from the LASCO/C2 coronagraph ($t_{cme} - 2h < t_{flare} < t_{cme} + 30$ min). The broad window for automatic selection was chosen so as to not accidentally eliminate a CME/flare combination before we manually checked it. We found 946 CMEs following our criteria during the given time period of observation by SDO. For each of the 946 automatically selected CMEs, we manually verified the following:

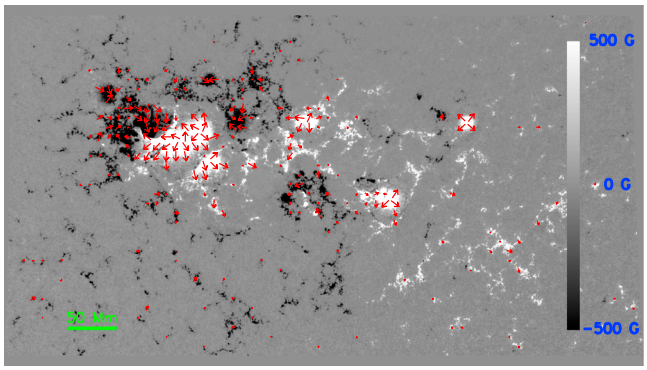

Figure 2. An example deprojected HARP-tile vector magnetogram containing NOAA AR 11520, which produced the X-class flare and CME shown in Figure 1. The size and direction of red vectors, overplotted on the grey-scaled vertical-field magnetogram, show the magnitude and direction of the horizontal field. The longest/shortest vector is for 500/100 G field strength.

(1) the CME was not seen in the LASCO C2 before the flare took place, (2) the CME occurred in the same quadrant as the source AR, and (3) there was no second flare occurring in another AR at nearly the same time. If there was a second flaring AR, we further verified that it was not the source of the CME under investigation.

By looking at LASCO-C2 movies and GOES X-ray flux plots, we made sure that the prospective flaring source AR was present on the frontside of the Sun. By looking at STEREO A and B movies we ensured that the CME was directed toward Earth; it did not come from a source on the back of the Sun. Far-side CMEs were discarded. We then used Atmospheric Imaging Assembly (AIA) 193 Å movies to determine which AR flare (out of sometimes several listed) was coproduced with the CME under investigation. The selection procedure for an example CME is illustrated in Figure 1. The movies (both for STEREO A and B and AIA 193) for the example event, shown in Figure 1, can be found at: http://cdaw.gsfc.nasa.gov/CME_list/daily_movies/2012/07/12/.

This careful manual selection procedure left a sample of 252 CMEs, with known flaring source ARs. The sample was further reduced by the requirement that there was available a definitive Helioseismic and Magnetic Imager (HMI) AR Patch (HARP) vector magnetogram that covered the source AR, which was taken within 12 h of the CME flare and which had its magnetic flux centroid (defined below) within 45 heliocentric degrees of disk center. We also required that the source AR (1) be the only NOAA AR in the HARP tile, (2) the values of parameters are mostly ($\geq$ 90%) from the AR and only negligibly ($\leq$ 10%) from the other parts of the tile, or (3) if many ARs exist in the HARP, they are closely merged together and can be treated as one AR. This left a sample of 189 CMEs that we finally kept for our study.

We use the HARP vector magnetograms, which have better azimuthal disambiguation than the Space-Weather HMI AR Patches (SHARPs) [*Bobra et al.*, 2014]. From the HARP vector magnetograms, we measured the magnetic parameters described in the next section. The magnetograms have a pixel size of 0.5″ and a cadence of 12 min. We prefer HARP over SHARP because our purpose in this paper is to look for any relationship between magnetic parameters and speed of CMEs that might lead to improvements in ongoing/future forecasting tools, e.g., MAG4 [*Falconer et al.*, 2014], in contrast to the aim of devising a near real time tool for forecasting the speed of CMEs.

Each HARP was deprojected to disk center; i.e., LOS and transverse vector components were transformed to vertical and horizontal vector components and resampled to square pixels. Noise from transverse field and foreshortening is prohibitive when ARs are far from disk center. Therefore, we limit our sample to HARPs within 45 heliocentric degrees. Falconer et al. (2015, in preparation) lays out the center-to-limb increase in deprojection errors in detail and shows that the parameters studied here have acceptably small projection errors out to 45 heliocentric degrees.

In Figure 2, we display an example of a deprojected vector magnetogram tile. We have reduced noise in the measured parameters by using only pixels where the field components are above certain threshold values (see next section).

The CME speeds have been obtained from the online LASCO/CME catalog [*Gopalswamy et al.*, 2009]. We use the speeds that are obtained from the linear fits to the height-time plot of the CME front in the plane of the

sky [*Yashiro et al.*, 2004; *Gopalswamy et al.*, 2009]. The uncertainty in this measurement of the speed is less than 10% [*Yashiro et al.*, 2004; *Gopalswamy et al.*, 2012, S. Yashiro, private communication, 2015]. This is apart from the basic deficiency of using 2-D images in contrast to using speeds calculated from 3-D reconstruction of the CMEs [e.g., *Joshi and Srivastava*, 2011; *Mishra and Srivastava*, 2013]. The difference between the true speed and the measured plane-of-sky speed is found to be more for the CMEs with smaller widths [e.g., *Gopalswamy et al.*, 2012, Yashiro, private communication, 2015]. As mentioned before, our CMEs are wider than 30°, therefore not exposed to larger error from projection on the plane of sky. We have included both halo and nonhalo CMEs to investigate the general correspondence between the speed of CMEs and the magnetic nonpotentiality of the source ARs. Because the CME speeds used are plane-of-sky speeds, they are smaller than the true speeds of the CME fronts. It is worth mentioning here that the estimation of true speeds of Earth-directed CMEs is difficult. In a case study, by using stereoscopic observations, *Gopalswamy et al.* [2012] found the plane-of-sky speed measured by LASCO to be smaller by only 7.6% and 3.4% than the plane-of-sky speeds measured by STEREO-A and STEREO-B, respectively.

3. AR Magnetic Parameters Studied

3.1. AR Size Parameters

We use two AR size parameters. Both are integrals of all pixels that have absolute vertical magnetic field strength B_z greater than 100 G. The first is the total magnetic area A,

$$A = \int dA, \tag{1}$$

and the second is the total magnetic flux Φ,

$$\Phi = \int B_z dA. \tag{2}$$

3.2. Length of Strong-Field Neutral Line

The strong-field neutral-line length of an AR is defined by

$$L_S = \int dl, \tag{3}$$

where the integral is over all intervals of neutral lines in which the horizontal component of the potential field is greater than 150 G, and the interval separates opposite polarities of at least 20 G field strength [*Falconer et al.*, 2008]. These neutral-line intervals are used for the two other neutral-line-length parameters, which are free-energy proxies, described in section 3.4.

To avoid magnetic parameters being dominated by noise, in this study we measure only ARs that are what we define to be strong-field ARs. Our definition follows *Falconer et al.* [2009]: a strong-field AR is one for which the ratio of L_S to the square root of the magnetic area A is greater than 0.7.

3.3. Global Twist Parameters

Global Alpha (α_g)**:** The magnetic twist parameter α measures the vertical gradient of magnetic twist (radians of twist per unit length of height) in each pixel of a deprojected AR vector magnetogram [see Appendix A of *Tiwari et al.*, 2009b]; see also *Leka and Skumanich* [1999]. A global value of α can be calculated using the following formula [e.g., *Tiwari et al.*, 2009b]:

$$\alpha_g = \frac{\sum \left(\frac{\partial B_y}{\partial x} - \frac{\partial B_x}{\partial y} \right) B_z}{\sum B_z^2}. \tag{4}$$

We use this direct way of obtaining global α because the singularities at neutral line are automatically avoided in this method by using the second moment of minimization. Only pixels with absolute B_z greater than 100 G are included in α_g.

Signed Shear Angle (SSA): Motivated by the presence of oppositely directed twists at small-scales in sunspot penumbrae, *Tiwari et al.* [2009a] proposed SSA, which measures magnetic twist in ARs irrespective of their

force-free nature [*Tiwari et al.*, 2009a] and shape [*Venkatakrishnan and Tiwari*, 2009]. It can be computed for each pixel of the deprojected vector magnetograms from the following formula:

$$\mathrm{SSA} = \tan^{-1}\left(\frac{B_{yo}B_{xp} - B_{yp}B_{xo}}{B_{xo}B_{xp} + B_{yo}B_{yp}}\right) \tag{5}$$

where B_{xo}, B_{yo}, and B_{xp}, B_{yp} are the observed and potential horizontal components of sunspot magnetic fields, respectively. The potential field is calculated from the vertical magnetic field using the method of *Alissandrakis* [1981]. Only pixels with absolute B_z greater than 100 G are used.

Spatially averaged SSA (SASSA) and the median of SSA (MSSA) are each a global magnetic twist parameter of an AR. The difference between the two is the following: noisy pixels contribute directly to SASSA, whereas they are least weighted for MSSA. Therefore, we have treated MSSA as a third global twist parameter here.

The SASSA and MSSA are both signed parameters; however, in the present study only magnitude is taken into account.

3.4. AR Free-Energy Proxies

Gradient-Weighted Neutral Line Length ($\mathbf{WL_{SG}}$): introduced by *Falconer et al.* [2008], this neutral line length measure is defined as

$$WL_{\mathrm{SG}} = \int |\nabla Bz| dl \tag{6}$$

where $|\nabla Bz|$ is the horizontal gradient of the vertical magnetic field. The integral is computed for all neutral-line intervals that separate opposite polarities of at least moderate field strength of 20 G and have horizontal potential field greater than 150 G. Please note that these cutoff values are based on those taken by *Falconer et al.* [2008] for Michelson Doppler Imager (MDI) data, and smaller numbers can be chosen for the HMI data. However, to be on the safe side, we have kept the same cutoff values in our present study.

Shear-Weighted Neutral Line Length ($\mathbf{WL_{SS}}$): also introduced in *Falconer et al.* [2008], this parameter is given by

$$WL_{\mathrm{SS}} = \int |\Phi - \Phi_p| dl \tag{7}$$

where Φ is the azimuth angle of the observed horizontal magnetic field and Φ_p is the azimuth angle of the potential horizontal magnetic field computed from the vertical magnetic field. The two free-energy proxies ($\mathrm{WL_{SG}}$ and $\mathrm{WL_{SS}}$) are strongly correlated and are being explored in another work to determine which parameter is better for flare prediction.

Schrijver's-R: *Schrijver* [2007] developed a free-energy proxy that measures the amount of flux near neutral line pixels. To obtain Schriver's-R, which we denote as $\mathrm{R_{Schr}}$, first, a neutral-line pixel map is determined. This is done by determining that all pixels are near a neutral line and that have positive or negative flux greater than 150 G. This step identifies strong-gradient neutral lines. This strong-gradient neutral-line-pixel map is then convolved with a 15 Mm Gaussian (as defined in *Schrijver* [2007] for MDI resolution). $\mathrm{R_{Schr}}$ is the unsigned flux in that area divided by that area, giving $\mathrm{R_{Schr}}$ a unit of G (Gauss). See *Schrijver* [2007], for more detail.

Net Current: The vertical current density J_z can be measured from a deprojected vector magnetogram using the following formula:

$$J_z = \frac{1}{\mu_0}\left(\frac{\partial B_y}{\partial x} - \frac{\partial B_x}{\partial y}\right). \tag{8}$$

An integration of J_z over all strong-field pixels ($|B_z| > 100$ G or $B_h > 200$ G) of an AR provides the net current for that AR. Following *Ravindra et al.* [2011], we use the sign convention that positive current flows upward in positive polarity regions and downward in negative polarity regions, with negative current having the opposite flow. To obtain the net current I_z, the net current in the positive polarity pixels, and the net current in the negative polarity pixels (see Figure 2), are added and divided by 2. This is the net current and not the total current since ARs can easily have, in one part of a polarity domain, positive current flowing and in other parts have negative current [e.g., *Ravindra et al.*, 2011].

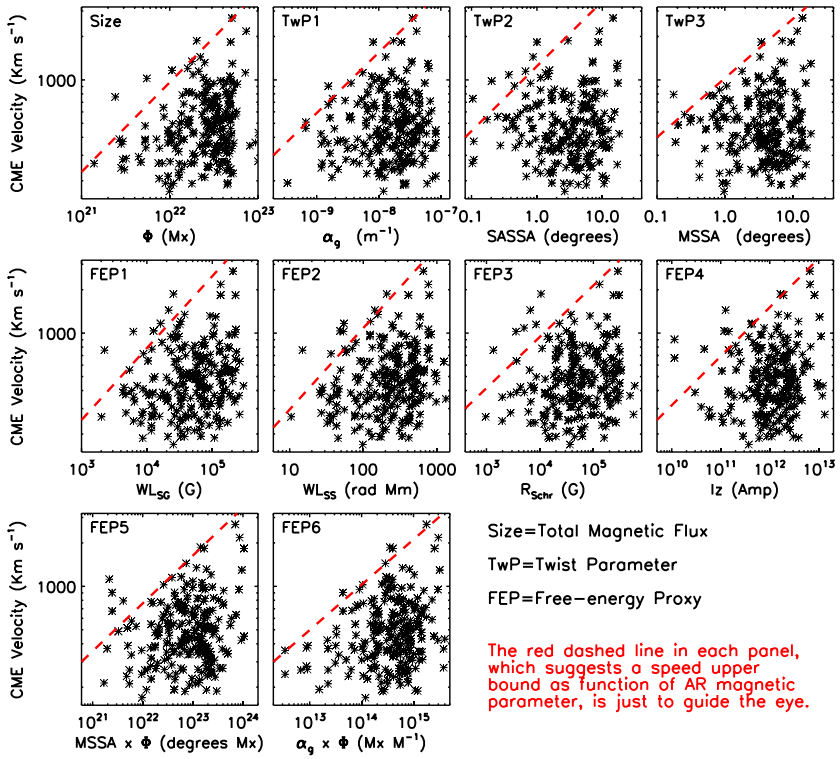

Figure 3. Scatterplots, in logarithmic scales on both *x* and *y* axes, of CME speed versus 10 different magnetic parameters of the source ARs. The first plot is for the AR's magnetic size (total magnetic flux Φ), the next three plots are for whole-AR magnetic twist parameters (α_g, **SASSA**, and **MSSA**), and the last six plots are for AR free-energy proxies ($\mathbf{WL}_{SG}$, $\mathbf{WL}_{SS}$, $\mathbf{R}_{Schr}$, $\mathbf{I}_z$, **MSSA**×Φ, and $\alpha_g \times \Phi$).

In addition to the above free-energy proxies, by multiplying by AR magnetic flux Φ, we converted the twist parameters α_g, SASSA, and MSSA to the AR free-energy proxies $\alpha_g \times \Phi$, SASSA ×Φ, MSSA ×Φ. This is meaningful because an AR with large twist but little total flux plausibly does not have enough free energy to produce fast CMEs, but an AR with the same large twist and large-enough flux plausibly does have enough free-energy to produce fast CMEs.

4. Results and Discussion

In Figure 3, total unsigned magnetic flux, three twist parameters, and six free-energy proxies (two of which are combinations of twist and flux) of ARs are plotted against the plane-of-sky speed of CMEs emanating from the ARs. For all the 10 plots in Figure 3 most data points fill a triangle portion of the phase space. Dashed red lines, drawn by eye following *Venkatakrishnan and Ravindra* [2003] (see dashed line in their Figure 3), outline the triangle area in each panel to roughly trace the upper bound of the speeds of CMEs.

Three important features in the plots that determine how well the speed of the fastest CMEs arising from an AR can be predicted are the following: (1) the *y* intercept of the red dashed line, (2) number of outliers above the line, and (3) how far above in *y* direction the outliers are from the line. By the *y* intercept of the red dashed line in each plot of Figure 3, we mean the *y* value at the point of intersection of the dashed line with the *y* axis of that plot (the left side of the box).

The triangular shape of the clouds of plotted points shows that the ARs with large nonpotentiality and large total flux produce both fast and slow CMEs, whereas ARs with the lower nonpotentiality and less flux produce only slower CMEs. This behavior is similar to the behavior that the most nonpotential ARs capable of producing large X-class flares also produce many smaller M- and C-class flares and ARs with relatively small nonpotentiality rarely if ever produce larger flares [e.g., *Tiwari et al.*, 2010].

For most plots there are a few outliers that are above the line. For two plots, α_g and $\alpha_g \times \Phi$, the upper limit line is not strongly violated, and the upper limit CME velocity for the smallest of these two parameters (*y* intercept)

is ~300 km s^{-1}. The number of outliers and their distance in *y* direction from the line is least for these two parameters. The magnetic flux plot shows a limit line of similar low *y* intercept but has more outliers, which are relatively farther in *y* direction above the limit line.

For the two better performing parameters, α_g and $\alpha_g \times \Phi$, the red dashed lines in Figure 3 give

$$v = 10^{(2.48 + 0.42 \times \log_{10}(\alpha_g / 2 \times 10^{-10}))} \text{ km s}^{-1} \text{ and} \quad (9)$$

$$v = 10^{(2.48 + 0.31 \times \log_{10}(\alpha_g \times \Phi / 2 \times 10^{12}))} \text{ km s}^{-1}, \text{ respectively.} \quad (10)$$

Because the lines are drawn by eye, they are not the only ones that could be drawn. By drawing different limit lines, however, we find no improvements in the predictive capabilities of the other eight parameters. For example, a less steep slope on free-energy proxy 4 (Figure 3) can reduce the number of outliers, but it also increases the *y* intercept of the limit line significantly. Similarly, the steepness of line can be increased in plots of the other seven of the eight parameters but that increases the number of outliers.

The α_g limit line has a lower *y* intercept, and all of outliers are as close or closer to the limit line in *y* direction, than for other two twist parameters, of which MSSA does better than SASSA. The fact that the α_g is weighted by strong magnetic field values and not affected by singularities at neutral lines [*Tiwari et al.*, 2009b, 2009a] might be responsible for its superior behavior over the other two twist parameters. The MSSA does better than the SASSA probably because while taking median, a few noisy pixels with extremely high values of SSA are suppressed whereas they contribute more to SASSA.

The neutral-length free-energy proxies do not directly include the full area of the ARs [*Falconer et al.*, 2008] and display some outliers. The same is true for R_{Schr}. The limit line for net current shows a number of outliers. The net current varies from zero to nonzero values [*Venkatakrishnan and Tiwari*, 2009; *Ravindra et al.*, 2011; P. Vemareddy et al., Flux emergence in the solar active region NOAA 11158: The evolution of net current, arXiv:1502.05458, 2015] in different phases of AR's lifetime. The evolution of net current could possibly explain why this free-energy proxy is not the best for predicting the upper speed limit of CMEs in a statistical sense.

The current solar cycle has been weak, and we do not have many CMEs faster than 1000 km^{-1} in our sample. By extending the sample as more data becomes available in the LASCO/CME catalog we will determine if this result is robust, or if the speed limit edge for α_g and $\alpha_g \times \Phi$ in Figure 3 becomes less sharp.

From the results of *Venkatakrishnan and Ravindra* [2003] and *Liu* [2007], we expect the free-energy proxies to better determine the upper speed limit of CMEs that an AR can produce than twist parameters do. The fact that the twist parameter α_g displays nearly similar limit line as its corresponding free-energy proxy $\alpha_g \times \Phi$ is surprising and remains to be explained.

In line with our observations, numerical simulations also suggest that the same ARs can produce both fast and slow CMEs, with the most complex ones producing the fastest CMEs [see, e.g., *Török and Kliem*, 2007]. The origin of slow CMEs from ARs with large nonpotentiality can probably be explained by the fact that oftentimes only a part of AR takes part in the eruption leading to a CME, and the full nonpotentiality of the AR does not drive those CMEs. However, identifying the exact part of the ARs that produces a flare/CME is not an easy task due to their complex magnetic structuring.

In the present analysis, we have used free-energy proxies instead of computing free magnetic energy itself that requires vector magnetograms measured in the force-free field above the photosphere, which are not available owing to instrumental limitations and also to the lack of reliable STOKE's profiles inversion codes for nonlocal thermodynamic equilibrium (NLTE) atmospheres. This limitation can be partially overcomed by reliable nonlinear force-free field modeling [*Wiegelmann and Sakurai*, 2012; *Wiegelmann et al.*, 2014] based on the photospheric vector field measurements of ARs, which are not entirely force-free on the AR photosphere [*Metcalf et al.*, 1995; *Tiwari*, 2012] but can be preprocessed to make them force-free under certain circumstances. Future studies should make use of such techniques to improve the accuracy of the prediction of the upper speed limit of the CMEs that an AR can produce.

5. Conclusions

In this letter, we investigated the correspondence between the speed of CMEs and nonpotentiality of their source ARs by using a total of 189 CMEs.

Plane-of-sky speed of CMEs was taken from the SOHO/LASCO CME catalog. In addition to total unsigned magnetic flux, various magnetic twist parameters and free-energy proxies of the source ARs were measured to gauge their nonpotentiality. To measure these parameters, HARP vector magnetograms from HMI were used after deprojection onto the solar disk center.

We find a general trend among all parameters that the ARs with larger nonpotentiality and total magnetic flux can produce both fast and slow CMEs, whereas the ARs with smaller nonpotentiality and flux can only produce slower CMEs. There are exceptions present for all of the parameters. Out of all the parameters studied, α_g and $\alpha_g \times \Phi$ show the best triangular pattern with least outliers, and lowest y intercept of the limit line, thus conveying their better performance over the other parameters for predicting the upper limit of the speed of CMEs that an AR can produce.

Since fast CMEs tend to be a greater threat for severe space weather than slower ones, knowing that an AR cannot produce a fast CME would be a useful forecast. Thus, our results can be incorporated in near real time forecasting tools e.g., MAG4 [*Falconer et al.*, 2014]. Expanding the data set of CMEs having measured speeds and measurable source ARs in future will improve statistics and confirm or modify our results.

Acknowledgments

S.K.T would like to thank Tibor Török and Yang Liu for the useful discussion on this work during the AGU-2014 meeting. We acknowledge Phyllis Whittlesey and Malte Broese, students from Joint Space Weather Summer Camp 2014 (sponsored by the University of Alabama in Huntsville and its Center for Space Plasma and Aeronomic Research, University of Rostock and its Leibniz-Institute of Atmospheric Physics, and the German Aerospace Center (DLR)), for initially identifying some of the CMEs and their source ARs. S.K.T. is supported by an appointment to the NASA Postdoctoral Program at the NASA MSFC, administered by ORAU through a contract with NASA. R.L.M. and A.R.W. are supported by funding from the LWS TRT Program of the Heliophysics Division of NASAs SMD. Support for MAG4 development comes from NASA's Game Changing Development Program and Johnson Space Center's Space Radiation Analysis Group (SRAG). Use of SOHO LASCO CME catalog, and data from AIA and HMI (SDO), STEREO, and SOHO are sincerely acknowledged. The CME catalog is generated and maintained at the CDAW Data Center by NASA and The Catholic University of America in cooperation with the NRL. SOHO is a project of international cooperation between ESA and NASA.

The Editor thanks two anonymous reviewers for their assistance in evaluating this paper.

References

Alissandrakis, C. E. (1981), On the computation of constant alpha force-free magnetic field, *Astron. Astrophys.*, *100*, 197–200.

Bein, B. M., S. Berkebile-Stoiser, A. M. Veronig, M. Temmer, and B. Vršnak (2012), Impulsive acceleration of coronal mass ejections: II. Relation to soft x-ray flares and filament eruptions, *Astrophys. J.*, *755*, 44, doi:10.1088/0004-637X/755/1/44.

Bobra, M. G., and S. Couvidat (2015), Solar flare prediction using SDO/HMI vector magnetic field data with a machine-learning algorithm, *Astrophys. J.*, *798*, 135, doi:10.1088/0004-637X/798/2/135.

Bobra, M. G., X. Sun, J. T. Hoeksema, M. Turmon, Y. Liu, K. Hayashi, G. Barnes, and K. D. Leka (2014), The Helioseismic and Magnetic Imager (HMI) Vector magnetic field pipeline: SHARPs — space-weather HMI active region patches, *Sol. Phys.*, *289*, 3549–3578, doi:10.1007/s11207-014-0529-3.

Burkepile, J. T., A. J. Hundhausen, A. L. Stanger, O. C. St. Cyr, and J. A. Seiden (2004), Role of projection effects on solar coronal mass ejection properties: 1. A study of CMEs associated with limb activity, *J. Geophys. Res.*, *109*, A03103, doi:10.1029/2003JA010149.

Canfield, R. C., H. S. Hudson, and D. E. McKenzie (1999), Sigmoidal morphology and eruptive solar activity, *Geophys. Res. Lett.*, *26*, 627–630, doi:10.1029/1999GL900105.

Dumbović, M., A. Devos, B. Vršnak, D. Sudar, L. Rodriguez, D. Ruždjak, K. Leer, S. Vennerstrøm, and A. Veronig (2015), Geoeffectiveness of coronal mass ejections in the SOHO Era, *Sol. Phys.*, *290*, 579–612, doi:10.1007/s11207-014-0613-8.

Falconer, D. A., R. L. Moore, and G. A. Gary (2002), Correlation of the coronal mass ejection productivity of solar active regions with measures of their global nonpotentiality from vector magnetograms: Baseline results, *Astrophys. J.*, *569*, 1016–1025, doi:10.1086/339161.

Falconer, D. A., R. L. Moore, and G. A. Gary (2008), Magnetogram measures of total nonpotentiality for prediction of solar coronal mass ejections from active regions of any degree of magnetic complexity, *Astrophys. J.*, *689*, 1433–1442, doi:10.1086/591045.

Falconer, D. A., R. L. Moore, G. A. Gary, and M. Adams (2009), The "Main Sequence" of explosive solar active regions: Discovery and interpretation, *Astrophys. J. Lett.*, *700*, L166–L169, doi:10.1088/0004-637X/700/2/L166.

Falconer, D. A., R. L. Moore, A. F. Barghouty, and I. Khazanov (2014), MAG4 versus alternative techniques for forecasting active region flare productivity, *Space Weather*, *12*, 306–317, doi:10.1002/2013SW001024.

Georgoulis, M. K., and D. M. Rust (2007), Quantitative forecasting of major solar flares, *Astrophys. J. Lett.*, *661*, L109–L112, doi:10.1086/518718.

Gopalswamy, N., S. Yashiro, and S. Akiyama (2007), Geoeffectiveness of halo coronal mass ejections, *J. Geophys. Res.*, *112*, A06112, doi:10.1029/2006JA012149.

Gopalswamy, N., S. Yashiro, G. Michalek, G. Stenborg, A. Vourlidas, S. Freeland, and R. Howard (2009), The SOHO/LASCO CME catalog, *Earth Moon Planets*, *104*, 295–313, doi:10.1007/s11038-008-9282-7.

Gopalswamy, N., S. Akiyama, S. Yashiro, and P. Mäkelä (2010), Coronal mass ejections from sunspot and non-sunspot regions, in *Magnetic Coupling Between the Interior and Atmosphere of the Sun*, edited by S. S. Hasan and and R. J. Rutten, pp. 289–307, Springer, Berlin, doi:10.1007/978-3-642-02859-5_24.

Gopalswamy, N., P. Makela, S. Yashiro, and J. M. Davila (2012), The relationship between the expansion speed and radial speed of CMEs confirmed using quadrature observations of the 2011 February 15 CME, *Sun and Geosphere*, *7*, 7–11.

Guo, J., H. Q. Zhang, and O. V. Chumak (2007), Magnetic properties of are-CME productive active regions and CME speed, *Astron. Astrophys.*, *462*, 1121–1126, doi:10.1051/0004-6361:20065888.

Hagyard, M. J., D. Teuber, E. A. West, and J. B. Smith (1984), A quantitative study relating observed shear in photospheric magnetic fields to repeated flaring, *Sol. Phys.*, *91*, 115–126, doi:10.1007/BF00213618.

Hoeksema, J. T., et al. (2014), The Helioseismic and Magnetic Imager (HMI) vector magnetic field pipeline: Overview and performance, *Sol. Phys.*, *289*, 3483–3530, doi:10.1007/s11207-014-0516-8.

Jing, J., C. Tan, Y. Yuan, B. Wang, T. Wiegelmann, Y. Xu, and H. Wang (2010), Free magnetic energy and flare productivity of active regions, *Astrophys. J.*, *713*, 440–449, doi:10.1088/0004-637X/713/1/440.

Joshi, A. D., and N. Srivastava (2011), Acceleration of coronal mass ejections from three-dimensional reconstruction of STEREO images, *Astrophys. J.*, *739*, 8, doi:10.1088/0004-637X/739/1/8.

Leka, K. D., and G. Barnes (2007), Photospheric magnetic field properties of flaring versus flare-quiet active regions. IV. A statistically significant sample, *Astrophys. J.*, *656*, 1173–1186, doi:10.1086/510282.

Leka, K. D., and A. Skumanich (1999), On the value of 'αAR' from vector magnetograph data: I. Methods and caveats, *Sol. Phys.*, *188*, 3–19.

Liu, Y. (2007), The speed of halo Coronal Mass Ejections and properties of associated active regions, *Adv. Space Res.*, *39*, 1767–1772, doi:10.1016/j.asr.2007.03.043.

Metcalf, T. R., L. Jiao, A. N. McClymont, R. C. Canfield, and H. Uitenbroek (1995), Is the solar chromospheric magnetic field force-free?, *Astrophys. J.*, *439*, 474–481, doi:10.1086/175188.

Mishra, W., and N. Srivastava (2013), Estimating the arrival time of Earth-directed coronal mass ejections at in situ spacecraft using COR and HI observations from STEREO, *Astrophys. J.*, *772*, 70, doi:10.1088/0004-637X/772/1/70.
Moore, R. L., D. A. Falconer, and A. C. Sterling (2012), The limit of magnetic-shear energy in solar active regions, *Astrophys. J.*, *750*, 24, doi:10.1088/0004-637X/750/1/24.
Ravindra, B. (2004), Evolution of magnetic fields in the solar atmosphere, PhD thesis, Indian Inst. of Astrophys., Bangalore Univ., India.
Ravindra, B., P. Venkatakrishnan, S. K. Tiwari, and R. Bhattacharyya (2011), Evolution of currents of opposite signs in the flare-productive solar active region NOAA 10930, *Astrophys. J.*, *740*, 19, doi:10.1088/0004-637X/740/1/19.
Schou, J., et al. (2012), Design and ground calibration of the Helioseismic and Magnetic Imager (HMI) instrument on the Solar Dynamics Observatory (SDO), *Sol. Phys.*, *275*, 229–259, doi:10.1007/s11207-011-9842-2.
Schrijver, C. J. (2007), A characteristic magnetic field pattern associated with all major solar flares and its use in flare forecasting, *Astrophys. J. Lett.*, *655*, L117–L120, doi:10.1086/511857.
Schrijver, C. J. (2009), Driving major solar ares and eruptions: A review, *Adv. Space Res.*, *43*, 739–755, doi:10.1016/j.asr.2008.11.004.
Srivastava, N., and P. Venkatakrishnan (2002), Relationship between CME speed and geomagnetic storm intensity, *Geophys. Res. Lett.*, *29*(9), 1287, doi:10.1029/2001GL013597.
Subramanian, P., and K. P. Dere (2001), Source regions of coronal mass ejections, *Astrophys. J.*, *561*, 372–395, doi:10.1086/323213.
Tiwari, S. K. (2012), On the force-free nature of photospheric sunspot magnetic fields as observed from Hinode (SOT/SP), *Astrophys. J.*, *744*, 65, doi:10.1088/0004-637X/744/1/65.
Tiwari, S. K., P. Venkatakrishnan, and K. Sankarasubramanian (2009a), Global twist of sunspot magnetic fields obtained from high-resolution vector magnetograms, *Astrophys. J. Lett.*, *702*, L133–L137, doi:10.1088/0004-637X/702/2/L133.
Tiwari, S. K., P. Venkatakrishnan, S. Gosain, and J. Joshi (2009b), Effect of polarimetric noise on the estimation of twist and magnetic energy of force-free fields, *Astrophys. J.*, *700*, 199–208, doi:10.1088/0004-637X/700/1/199.
Tiwari, S. K., P. Venkatakrishnan, and S. Gosain (2010), Magnetic non-potentiality of solar active regions and peak X-ray flux of the associated flares, *Astrophys. J.*, *721*, 622–629, doi:10.1088/0004-637X/721/1/622.
Török, T., and B. Kliem (2007), Numerical simulations of fast and slow coronal mass ejections, *Astron. Nachr.*, *328*, 743–746, doi:10.1002/asna.200710795.
Venkatakrishnan, P., and B. Ravindra (2003), Relationship between CME velocity and active region magnetic energy, *Geophys. Res. Lett.*, *30*(23), 2181, doi:10.1029/2003GL018100.
Venkatakrishnan, P., and S. K. Tiwari (2009), On the absence of photospheric net currents in vector magnetograms of sunspots obtained from Hinode (solar optical telescope/spectro-polarimeter), *Astrophys. J. Lett.*, *706*, L114–L119, doi:10.1088/0004-637X/706/1/L114.
Vršnak, B., D. Sudar, and D. Ruždjak (2005), The CME-flare relationship: Are there really two types of CMEs?, *Astron. Astrophys.*, *435*, 1149–1157, doi:10.1051/0004-6361:20042166.
Wang, Y., and J. Zhang (2008), A statistical study of solar active regions that produce extremely fast coronal mass ejections, *Astrophys. J.*, *680*, 1516–1522, doi:10.1086/587619.
Wiegelmann, T., and T. Sakurai (2012), Solar force-free magnetic fields, *Living Rev. Sol. Phys.*, *9*, 5, doi:10.12942/lrsp-2012-5.
Wiegelmann, T., J. K. Thalmann, and S. K. Solanki (2014), The magnetic field in the solar atmosphere, *Astron. Astrophys.*, *22*, 78, doi:10.1007/s00159-014-0078-7.
Yashiro, S., N. Gopalswamy, G. Michalek, O. C. St. Cyr, S. P. Plunkett, N. B. Rich, and R. A. Howard (2004), A catalog of white light coronal mass ejections observed by the SOHO spacecraft, *J. Geophys. Res.*, *109*, A07105, doi:10.1029/2003JA010282.
Yashiro, S., G. Michalek, S. Akiyama, N. Gopalswamy, and R. A. Howard (2008), Spatial relationship between solar flares and coronal mass ejections, *Astrophys. J.*, *673*, 1174–1180, doi:10.1086/524927.
Zirin, H., and M. A. Liggett (1987), Delta spots and great flares, *Sol. Phys.*, *113*, 267–281, doi:10.1007/BF00147707.